Electronic Research Archive

https://www.aimspress.com/journal/era

ERA, 34(2): 1269–1289.
DOI: 10.3934/era.2026058
Received: 22 November 2025
Revised: 10 January 2026
Accepted: 20 January 2026
Published: 06 February 2026

Research article

A characteristics finite element method for incompressible flow based on two local Gauss integrations

Yu Jiang, Junchang Qin*, Huipeng Gu and Xiujuan Zhao

Shenzhen University of Information Technology, Shenzhen 518172, China

* **Correspondence:** Email: qinjc@suit-sz.edu.cn.

Abstract: This study investigates a numerical method for incompressible flows governed by unsteady Navier–Stokes equations, proposing a characteristic finite element method based on two Gauss integrations. The proposed method is compared and analyzed with the classical two-grid method and variational multiscale methods, respectively, with error estimates conducted. The superiority of the characteristic finite element method based on two Gauss integrations is verified through numerical examples with exact solutions. For a high Reynolds number of 10^6, both algorithms remain stable. The computational results show strong agreement with those reported in well-established literature. Furthermore, simulations of the lid-driven cavity flow are performed, and the computational results are in excellent agreement with those of Ghia Ghia and Shin.

Keywords: two local Gauss integrations; Navier–Stokes; incompressible flow; characteristics

1. Introduction

For an incompressible fluid flow, we consider a bounded convex domain $\Omega \subset \mathbb{R}^2$ with a Lipschitz-continuous boundary $\partial\Omega$ and a finite time interval $(0, T)$. Standard notation for norms and seminorms in Sobolev spaces is adopted throughout this work. The convective velocity field $\mathbf{u}$ and the pressure p are obtained as the solution of the time-dependent incompressible Navier–Stokes equations (NS), which takes the following form:

$$\begin{cases} \frac{\partial u}{\partial t} - 2\nu\nabla \cdot D(u) + (u \cdot \nabla u) + \nabla p = f, & \text{in } \Omega \times (0, \mathrm{T}], \\ \nabla \cdot u = 0 & \text{in } \Omega \times (0, \mathrm{T}], \\ u(0) = u_0 & \text{on } \Omega \times \{0\}, \\ u = 0 & \text{on } \partial\Omega \times (0, \mathrm{T}], \end{cases} \tag{1.1}$$

where $D(u) = (\nabla u + \nabla u^T)/2$ is the velocity deformation tensor. f is denoted for the external force. u_0 represents the initial velocity of system (1.1) at time zero. Several scientifically valid

and effective algorithms have been proposed for the incompressible Navier–Stokes equations, such as the two stabilized finite element methods based on local polynomial pressure projections [1], two-level iterative finite element methods [2], evolving interfaces without re-meshing processes or regularization [3], a split-step scheme in conjunction with the standard finite-element method [4], and a linearized, fully discrete, arbitrary Lagrangian–Eulerian finite element method [5]. Spatial error is estimated by evaluating finite element residuals and jump terms across element boundaries, while temporal discretization error is assessed via reconstructions to better approximate continuous solutions and guide time-step refinement [6]. An immersed Petrov–Galerkin formulation is implemented on a uniform Cartesian mesh that does not conform to the interface [7]. The multiscale finite element methods [8–14], and others [15–17], have proven effective for tackling problems featuring disparate spatial or temporal scales.

This work presents a comparative analysis of four different finite element schemes for the time-dependent Navier–Stokes equations. The most effective algorithm is subsequently selected for a detailed study of its stability and error estimates. Here, we first introduce some notations:

$$X = H_0^1(\Omega)^2, \;\; Y = L^2(\Omega)^2, \;\; M = L_0^2(\Omega), \;\; V = \{v \in X : \; \nabla \cdot v = 0\}.$$

$$D(A) = H^2(\Omega)^2 \cap V, \;\; H = \{v \in H_0^1(\Omega)^2 \mid \; \nabla \cdot v = 0 \text{ in } \Omega \text{ and } v \cdot n = 0\}.$$

$$L^\alpha(0,T;X) = \{v : t_1 ..., t_N \to X \mid\mid\mid v\|_{L^\alpha(0,T;X)} = [\Delta t \sum_{i=1}^{N} \|v(t_i)\|_X^\alpha]\frac{1}{\alpha} < \infty\}, \; 1 \le \alpha < \infty.$$

$$L^\infty(0,T;X) = \{v : t_1 ..., t_N \to X \mid \|v\|_{L^\infty(0,T;X)} = \max_{1\le i\le N} \|v(t_i)\|_X < \infty\}.$$

We define a generalized bilinear form on the product space $(X, M) \times (X, M)$ as follows:

$$B_0((u,p);(v,q)) = a(u,v) - d(v,p) + d(u,q).$$

The continuous bilinear forms $a(\cdot,\cdot)$ and $d(\cdot,\cdot)$ along with the trilinear form $b(\cdot,\cdot,\cdot)$ are defined on $X \times X$ and $X \times M$, respectively, by

$$a(u,v) = \nu(\nabla u, \nabla v), \quad d(v,q) = (\nabla \cdot v, q) = -(v, \nabla q).$$

$$b(u,v,w) = \int_\Omega (u \cdot \nabla)v \cdot w \mathrm{dx}.$$

The norm in $L^2(\Omega)^2$ is denoted by $\|\cdot\|_0$, and the norm in the standard Sobolev space $H^k(\Omega)^2$ is denoted by $\|\cdot\|_k$. The space X is equipped with the norm $\{(\nabla\cdot, \nabla\cdot)\}^{1/2}$ or $\|\cdot\|_1$, and Q is endowed with the standard L^2 norm.

Let $0 < h < H$ and define $\widetilde{h} = h$ or H. The mesh size is given by $\widetilde{h} = \max_{\Omega_e \in \tau_{\widetilde{h}}} \mathrm{diam}(\Omega_e)$, where β is a constant independent of $\widetilde{h}$.

We consider the low-order P_1–P_1 finite element pair

$$X_{\widetilde{h}} = \left\{u_{\widetilde{h}} \in C(\Omega)^2 \mid u_{\widetilde{h}}|_{\Omega_e} \in P_1(\Omega_e)^2, \quad \forall \Omega_e \in \tau_{\widetilde{h}}\right\},$$
$$Q_{\widetilde{h}} = \left\{q_{\widetilde{h}} \in C(\Omega) \mid q_{\widetilde{h}}|_{\Omega_e} \in P_1(\Omega_e), \quad \forall \Omega_e \in \tau_{\widetilde{h}}\right\}.$$

We also introduce the piecewise constant space

$$R_0 = \left\{ v_{\widetilde{h}} \in L^2(\Omega) \mid v_{\widetilde{h}}|_{\Omega_e} \in P_0(\Omega_e), \quad \forall \Omega_e \in \tau_{\widetilde{h}} \right\},$$

where $P_0(\Omega_e)$ denotes the space of constant polynomials on Ω_e.

Furthermore, we define two tensor-valued spaces: $L = L^2(\Omega)^{2\times 2}$ and $L_{\widetilde{h}} = R_0(\Omega)^{2\times 2}$. The latter is defined on the same mesh as the velocity deformation tensor space $X_{\widetilde{h}}$.

This paper is organized as follows. In Section 2, the characteristic finite element algorithm based on two local Gauss integrations is proposed and briefly analyzed. In Section 3, a review of some classical finite element algorithms for the unsteady Navier–Stokes equations are provided, such as the variational multiscale (VMS) finite element method and the two-grid finite element method (TGFEM), numerical experiments. In Section 4, the conclusion is drawn.

2. Characteristics finite element method based on two local Gauss integrations

In this section, we will recall the traditional characteristic finite element method for the Navier–Stokes model [18, 19]. The finite element subspaces used in this paper are the continuous piecewise bilinear velocity subspace

$$X_{\widetilde{h}} = \{v = (v_1, v_2) \in C^0(\bar{\Omega})^2 \cap X : v_i \mid_K \in P_1(K)\ \forall K \in \Omega_e, i = 1, 2\}$$

and the linear pressure subspace

$$M_{\widetilde{h}} = \{q \in C^0(\bar{\Omega}) \cap M : \ q \mid_K \in P_1(K)\ \forall K \in \Omega_e\}.$$

Here, Ω_e is a triangulation of Ω into triangles or quadrilaterals, assumed to be regular in the usual sense, and $P_1(K)$ is the set of all polynomials on K of degree less than or equal to one.

The characteristic finite element method is based on two local Gauss integrations. We first review the characteristic finite element method and then introduce a stabilization term formulated through local Gauss integration. This leads to the development of a characteristic finite element scheme, incorporating two local Gauss integrations, for solving the time-dependent Navier–Stokes equations.

Let $\psi(x,t) = (1+ \mid u \mid^2)^{\frac{1}{2}}$, where $\mid u \mid^2 = u_1^2(x,t) + u_2^2(x,t)$. The characteristic direction $u_t + (u \cdot \nabla)u$ is denoted by τ [18, 19]. Then,

$$\frac{\partial}{\partial \tau} = \frac{1}{\psi(x,t)} \frac{\partial}{\partial t} + \frac{1}{\psi(x,t)} u \cdot \nabla,$$
$$D_t u = \psi(x,t) \frac{\partial u}{\partial \tau}.$$

Under the notations above, the mixed variational form of the momentum equation of problem (1.1) is to seek $(u, p) \in (X, M)$ such that

$$(D_t u, v) + B_0((u, p); (v, q)) = (f, v)\ \forall (v, q) \in (X, M). \tag{2.1}$$

Consider the backward difference along the τ characteristic tangent as the approximation of $\psi(x,t)\frac{\partial u}{\partial \tau}$. For an integer N, define the time step $\Delta t = \frac{T}{N}$ and discrete times $t^m = t_0 + m\Delta t$, $m = 0, 1, 2..., N$. Furthermore, we have

$$D_t u(x, t_m) \approx \psi(x,t) \frac{u(x, t^m) - u(\overline{x}, t^{m-1})}{\sqrt{(x - \overline{x})^2 + \Delta t^2}} = \frac{u^m - \overline{u}^{m-1}}{\Delta t},$$

where $\overline{x} = x - u(x, t^{m-1})\Delta t$.

The characteristic finite element discretization of the transient Navier–Stokes equations (1.1) seeks $(u_{\widetilde{h}}^{m+1}, p_{\widetilde{h}}^{m+1}) \in X_{\widetilde{h}} \times M_{\widetilde{h}}$ to satisfy, for all $(v_{\widetilde{h}}, q_{\widetilde{h}}) \in X_{\widetilde{h}} \times M_{\widetilde{h}}$,

$$(d_t u_{\widetilde{h}}^{m+1}, v_{\widetilde{h}}) + B_0((u_{\widetilde{h}}^{m+1}, p_{\widetilde{h}}^{m+1}); (v_{\widetilde{h}}, q_{\widetilde{h}})) = (f^{m+1}, v_{\widetilde{h}}), \tag{2.2}$$

where $d_t u_{\widetilde{h}}^{m+1}(x) = \frac{u_{\widetilde{h}}^{m+1}(x) - u_{\widetilde{h}}^{m}(X_{\widetilde{h}}^{m}(x, t_{m+1}; t_m))}{\Delta t}$, and $X(x, t_{m+1}; t)$ denotes the characteristic curves associated with the material derivative $D_t u$ [18, 19]. For all $(v_{\widetilde{h}}, q_{\widetilde{h}}) \in X_{\widetilde{h}} \times M_{\widetilde{h}}$, $X_{\widetilde{h}}^{m}(x, t_{m+1}; t_m)$ is the solution of

$$\begin{cases} \frac{\mathrm{dX_{\widetilde{h}}^{m}(x,t_{m+1};t)}}{dt} = u_{\widetilde{h}}^{m}(X_{\widetilde{h}}^{m}(x, t_{m+1}; t, t)), \quad t_m \le t \le t_{m+1}, \\ X_{\widetilde{h}}^{m}(x, t_{m+1}; t_{m+1}) = x. \end{cases}$$

Algorithm 1. Characteristic finite element method (CFEM) based on two Gauss integrations.

The Navier–Stokes equations are solved via the characteristic finite element method. This involves finding $(u_{\widetilde{h}}^{m+1}, p_{\widetilde{h}}^{m+1}) \in X_{\widetilde{h}} \times M_{\widetilde{h}}$ such that

$$(d_t u_{\widetilde{h}}^{m+1}, v_{\widetilde{h}}) + B_1((u_{\widetilde{h}}^{m+1}, p_{\widetilde{h}}^{m+1}); (v_{\widetilde{h}}, q_{\widetilde{h}})) = (f^{m+1}, v_{\widetilde{h}}), \quad (v_{\widetilde{h}}, q_{\widetilde{h}}) \in (X_{\widetilde{h}} \times M_{\widetilde{h}}), \tag{2.3}$$

$$B_1((u_{\widetilde{h}}^{m+1}, p_{\widetilde{h}}^{m+1}) = B_0((u_{\widetilde{h}}^{m+1}, p_{\widetilde{h}}^{m+1}) + G_1(u_{\widetilde{h}}, v_{\widetilde{h}}).$$

The introduction of the stabilization form, conceived as the difference between a consistent and an underintegrated mass matrix, is based on employing two local Gauss integrations per element:

$$G_1(u_{\widetilde{h}}, v_{\widetilde{h}}) = (a_k(u_{\widetilde{h}}, v_{\widetilde{h}}) - a_1(u_{\widetilde{h}}, v_{\widetilde{h}})).$$

Here,

$$\begin{aligned} &a_k(u_{\widetilde{h}}, v_{\widetilde{h}}) = u_G^T M_k v_G, \quad a_1(u_{\widetilde{h}}, v_{\widetilde{h}}) = u_G^T M_1 v_G, \\ &u_G^T = [u_1, u_2..., u_N]^T, \quad v_G = [v_1, v_2, ..., v_N], \\ &M_{ij} = (\nabla\phi_i, \nabla\phi_j), \quad u_{\widetilde{h}} = \sum_{i=1}^{N} u_i\phi_i, \quad u_i = u_h(x_i), \quad \forall u_{\widetilde{h}} \in X_{\widetilde{h}}, \quad i = 1, 2, ..., N, \\ &M_k = (M_{ij}^k)_{N\times N}, \quad M_1 = (M_{ij}^1)_{N\times N}; \end{aligned}$$

ϕ_i is the basis function of the velocity on the domain Ω such that its value is one at node x_i and zero at other nodes, and N is the dimension of $X_{\widetilde{h}}$. The symmetric and positive matrices M_{ij}^k, $k \ge 2$, and M_{ij}^1 are the stiffness matrices computed by using k-order and 1-order Gauss integrations at element level, respectively. u_i and v_i, $i = 1, 2, ..., N$ are the values of $u_{\widetilde{h}}$ and $v_{\widetilde{h}}$ at the node x_i. In detail, the stabilized term can be rewritten as

$$G_1(u_{\widetilde{h}}, v_{\widetilde{h}}) = \sum_{\Omega_e \in \tau_{\widetilde{h}}} \{\int_{\Omega_{e,k}} \nabla u_{\widetilde{h}} \nabla v_{\widetilde{h}} dx - \int_{\Omega_{e,1}} \nabla u_{\widetilde{h}} \nabla v_{\widetilde{h}} dx\}, \quad \forall u_{\widetilde{h}}, v_{\widetilde{h}} \in M_{\widetilde{h}}.$$

We make the regularity assumption that the corresponding solution (u, p) of problem (1.1) satisfies the following conditions.

Regularity hypotheses:

A. $u \in L^\infty(0, T, H^2(\Omega)^2) \bigcap C(C^{0,1}(\bar{\Omega})^2) \bigcap C(V)$

B. $\frac{du}{dt} \in L^2(H^2(\Omega)^2 \bigcap L^2(H)),\ \ D_t^2 u \in L^2(H)$

C. $p \in L^\infty(H^1(\Omega)) \bigcap L^\infty(L_0^2(\Omega)),\ \ \frac{dp}{dt} \in L^2(H^1(\Omega))$

Theorem 2.1. Let $(X_{\tilde{h}}, M_{\tilde{h}})$ be defined as above; there exists a positive constant β independent of h [18–20] such that

$$
\begin{aligned}
&| B((u,p);(v,q)) | \leq c(\| u \|_1 + \| p \|_0)(\| v \|_1 + \| q \|_0)\ (u,p),(v,q) \in (X,M).\\
&\beta(\| u_{\tilde{h}} \|_1 + \| p_{\tilde{h}} \|_0) \leq \sup_{(v_{\tilde{h}}, q_{\tilde{h}}) \in (X_{\tilde{h}}, M_{\tilde{h}})} \frac{|B((u_{\tilde{h}}, p_{\tilde{h}});(v_{\tilde{h}}, q_{\tilde{h}}))|}{\|v\|_1 + \|q\|_0} \quad \forall (u_{\tilde{h}}, p_{\tilde{h}}) \in (X_{\tilde{h}}, M_{\tilde{h}}).\\
&| G_1(u,v) | \leq C \| (I - II_{\tilde{h}})\nabla u \|_0 \| (I - II_{\tilde{h}})\nabla v \|_0 \ \ \forall u, v \in X.
\end{aligned}
$$

3. Error analysis of the characteristic finite element method (CFEM) based on two local Gauss integrations

As in [19, 20], taking $v_{\tilde{h}} = u_{\tilde{h}}^{m+1}, q_{\tilde{h}} = p_{\tilde{h}}^{m+1}$ in (2.3) yields

$$
\begin{aligned}
&\| u_{\tilde{h}}^{m+1} \|_0^2 + \nu\Delta t \| \nabla u_{\tilde{h}}^{m+1} \|_0^2 + \Delta t \| (I - \Pi_{\tilde{h}})\nabla u_{\tilde{h}}^{m+1} \|_0^2\\
&= \Delta t(f^{m+1}, u_{\tilde{h}}^{m+1}) + (u_{\tilde{h}}^m(X_{\tilde{h}}^m(x, t_{m+1}; t_m)), u_{\tilde{h}}^{m+1}).
\end{aligned}
$$

Using the Young inequality, we obtain

$$
\begin{aligned}
&(\| u_{\tilde{h}}^{m+1} \|_0^2 + \nu\Delta t \| \nabla u_{\tilde{h}}^{m+1} \|_0^2 + \Delta t \| (I - \Pi_{\tilde{h}})\nabla u_{\tilde{h}}^{m+1} \|_0^2)^{\frac{1}{2}}\\
&= \Delta t \| f^{m+1} \|_0^2 + \| u_{\tilde{h}}^m \|_0^2;
\end{aligned}
$$

further,

$$
\begin{aligned}
&(\| u_{\tilde{h}}^{m+1} \|_0^2 + \nu\Delta t \| \nabla u_{\tilde{h}}^{m+1} \|_0^2 + \Delta t \| (I - \Pi_{\tilde{h}})\nabla u_{\tilde{h}}^{m+1} \|_0^2)^{\frac{1}{2}}\\
&= \Delta t \| f^{m+1} \|_0^2 + (\| u_{\tilde{h}}^m \|_0^2 + \nu\Delta t \| \nabla u_{\tilde{h}}^m \|_0^2)^{\frac{1}{2}}.
\end{aligned}
$$

So,

$$
\begin{aligned}
&(\| u_{\tilde{h}}^{m+1} \|_0^2 + \nu\Delta t \| \nabla u_{\tilde{h}}^{m+1} \|_0^2)^{\frac{1}{2}}\\
&= \Delta t \| f^{m+1} \|_0^2 + (\| u_{\tilde{h}}^m \|_0^2 + \nu\Delta t \| \nabla u_{\tilde{h}}^m \|_0^2)^{\frac{1}{2}}.
\end{aligned}
$$

Based on the definitions above, we obtain the following approximation properties.

Lemma 4.1 [19,20]. For $\forall (u,p) \in (X,M)$, there holds

$$
\| R_{\tilde{h}}(u,p) - u \|_1 + \| Q_{\tilde{h}}(u,p) - p \|_0 \leq C(\| u \|_1 + \| p \|_0),
$$

and for $\forall (u,p) \in (D(A), H^1(\Omega) \cap M)$,

$$
\begin{aligned}
&\| R_{\tilde{h}}(u,p) - u \|_0 + h(\| R_{\tilde{h}}(u,p) - u \|_1 + \| Q_{\tilde{h}}(u,p) - p \|_0)\\
&\leq Ch^2(\| u \|_2 + \| p \|_1),
\end{aligned}
$$

where $D(A) = (H^2(\Omega)^2) \cap V$.

Theorem 4.1 Under regularity hypotheses, we have

$$
\| u - u_{\tilde{h}} \|_{L^\infty(L^2(\Omega)^2)} \leq C(\Delta t + h^2).
$$

Proof. Let $e = u - u_{\tilde{h}},\ \delta = u - R_{\tilde{h}}(u-p),\ \sigma = \delta - e = u_{\tilde{h}} - R_{\tilde{h}}(u,p),\ \eta = p_{\tilde{h}} - Q_{\tilde{h}}(u,p)$. Subtracting (2.3) from (2.1) with $(v,q) = (v_{\tilde{h}}, q_{\tilde{h}})$, we have

$$
\begin{aligned}
&(d_t\sigma^{m+1}, v_{\tilde{h}}) + a(\sigma^{m+1}, v_{\tilde{h}}) - d(v_{\tilde{h}}, \eta^{m+1}) + d(\sigma^{m+1}, q_{\tilde{h}})\\
&+ G_2(\sigma^{m+1}, v_{\tilde{h}}) = (D_t u - d_t u, v_{\tilde{h}}) + (d_t\delta^{m+1}, v_{\tilde{h}}).
\end{aligned} \tag{3.1}
$$

taking $v_{\widetilde{h}} = \sigma^{m+1},\ q_{\widetilde{h}} = \eta^{m+1}$ we then get

$$(d_t\sigma^{m+1}, \sigma^{m+1}) + \nu \parallel \nabla\sigma^{m+1} \parallel_0^2 + \parallel (I - \amalg_{\widetilde{h}})\nabla\sigma^{m+1} \parallel_0^2$$
$$= (D_t u(\cdot, t_{m+1}) - d_t u(\cdot, t_{m+1}), \sigma^{m+1}) + (d_t\delta(\cdot, t_{m+1}), \sigma^{m+1}).$$

From Theorem 4.1 of [19], we obtain

$$\begin{aligned}
&\frac{1}{2\Delta t}(\parallel \sigma^{m+1} \parallel_0^2 - \parallel \sigma^m \parallel_0^2) + \nu \parallel \nabla\sigma^{m+1} \parallel_0^2 + \parallel (I - \amalg_h)\nabla\sigma^{m+1} \parallel_0^2 \\
&\leq \varepsilon_1 \parallel \sigma^{m+1} \parallel_0^2 + \varepsilon_2 \parallel \nabla\sigma^{m+1} \parallel_0^2 + C\Delta t(\parallel D_t^2 u \parallel^2_{L^2(t_m, t_{m+1}; L^2(\Omega)^2)} + \\
&\parallel \frac{du}{dt} \parallel^2_{L^2(t_m, t_{m+1}; L^2(\Omega)^2)}) + \frac{C}{\Delta t} \parallel \frac{d\delta}{dt} \parallel^2_{L^2(t_m, t_{m+1}; L^2(\Omega)^2)} \\
&+ C \parallel e^m \parallel_0^2 + C \parallel \delta \parallel^2_{L^\infty(L^2(\Omega)^2)} + C \parallel \sigma^m \parallel_0^2 .
\end{aligned} \tag{3.2}$$

Upon multiplying inequality (3.2) by $2\Delta t$, summing over index m from 0 to n, and selecting $\varepsilon_1 = \frac{1}{4T}$, $\varepsilon_2 = \frac{\nu}{2}$, we derive the following recurrence relation.

$$\begin{aligned}
&\parallel \sigma^{n+1} \parallel_0^2 + \nu\Delta t \sum_{m=0}^{n+1} \parallel \nabla\sigma^m \parallel_0^2 + 2\Delta t \sum_{m=0}^{n} \parallel (I - \amalg_h)\nabla\sigma^{m+1} \parallel_0^2 \\
&\leq C\Delta t^2(\parallel D_t^2 u \parallel^2_{L^2(L^2(\Omega)^2)} + \parallel \frac{du}{dt} \parallel^2_{L^2(L^2(\Omega)^2)}) + C(\parallel \delta \parallel^2_{L^\infty(L^2(\Omega)^2)} \\
&+ \parallel \frac{d\delta}{dt} \parallel^2_{L^2(L^2(\Omega)^2)}) + C\Delta t \sum_{m=0}^{n} \parallel e^m \parallel_0^2 + C\Delta t \sum_{m=0}^{n} \parallel \sigma^m \parallel_0^2 .
\end{aligned} \tag{3.3}$$

An application of the discrete Grönwall's lemma and Lemma 4.1 yields

$$\begin{aligned}
&\parallel e^{n+1} \parallel_0^2 \leq 2 \parallel \sigma^{n+1} \parallel_0^2 + 2 \parallel \delta^{n+1} \parallel_0^2 \\
&\leq C\Delta t^2(\parallel D_t^2 u \parallel^2_{L^2(L^2(\Omega)^2)} + \parallel \frac{du}{dt} \parallel^2_{L^2(L^2(\Omega)^2)}) \\
&+ Ch^4(\parallel u \parallel^2_{L^\infty(H^2(\Omega)^2)} + \parallel \frac{du}{dt} \parallel^2_{L^2(L^2(\Omega)^2)} + \parallel p \parallel^2_{L^\infty(H^1(\Omega))} \\
&+ \parallel \frac{dp}{dt} \parallel^2_{L^2(H^1(\Omega))}) + C\Delta t \sum_{m=0}^{n} \parallel e^m \parallel_0^2 .
\end{aligned} \tag{3.4}$$

We thus conclude the proof by invoking the discrete Grönwall's lemma to obtain Theorem 4.1.

Theorem 4.2. Under the regularity hypothesis and condition $2C < \frac{\widetilde{h}^2}{\Delta t} < 1$, it holds that

$$\parallel u - u_{\widetilde{h}}(t_m) \parallel_{L^\infty(H^1(\Omega)^2)} \leq C(\Delta t + \widetilde{h}). \tag{3.5}$$

An optimal order estimate for $\parallel u - u_{\widetilde{h}} \parallel_{L^\infty(H^1(\Omega)^2)}$ can be derived in a similar fashion of Theorem 4.1. Taking $v_{\widetilde{h}} = \frac{\sigma^{m+1} - \sigma^m}{\Delta t},\ q_{\widetilde{h}} = \frac{\eta^{m+1}}{\Delta t}$ in (3.1), we have

$$
\begin{aligned}
&\| \frac{\sigma^{m+1}-\sigma^m}{\Delta t} \|_0^2 + \frac{\nu}{2\Delta t}(\| \nabla\sigma^{m+1} \|_0^2 - \| \nabla\sigma^m \|_0^2) + d(\frac{\sigma^m}{\Delta t}, \eta^{m+1}) \\
&+\frac{1}{\Delta t}(\| \nabla\sigma^{m+1} \|_0^2 - \| \nabla\sigma^m \|_0^2) + \frac{\nu}{2} \mid \frac{\sigma^{m+1}-\sigma^m}{(\Delta t)^{\frac{1}{2}}} \mid_1^2 \\
&\leq \varepsilon_3 \| \frac{\sigma^{m+1}-\sigma^m}{\Delta t} \|_0^2 + C\Delta t(\| D_t^2 u \|^2_{L^2(t_m,t_{m+1};L^2(\Omega)^2)} + \| \frac{du}{dt} \|^2_{L^2(t_m,t_{m+1};L^2(\Omega)^2)}) \\
&+\frac{C}{\Delta t} \| \frac{d\delta}{dt} \|^2_{L^2(t_m,t_{m+1};L^2(\Omega)^2)} + C \| e^m \|_0^2 + C \| \delta \|^2_{L^\infty(H^1(\Omega)^2)} \\
&+\varepsilon_4 \mid \frac{\sigma^{m+1}-\sigma^m}{(\Delta t)^{\frac{1}{2}}} \mid_1^2 + C(1+\frac{\alpha_m}{\Delta t}) \| \delta \|^2_{L^\infty(H^1(\Omega)^2)} + C \| \nabla\sigma \|_0^2 \\
&+C(1+\frac{\alpha_m}{\Delta t}) \| \nabla\sigma^m \|_0^2, \qquad (3.6)
\end{aligned}
$$

where, $\alpha_m = D_N(\widetilde{h})^2((\Delta t)^2 + \Delta t \| \frac{du}{dt} \|^N_{L^2(t_m,t_{m+1};L^2(\Omega)^2)}), D_N(\widetilde{h}) = \widetilde{h}^{1-\frac{1}{N}}(\log\frac{1}{\widetilde{h}})^{1-\frac{1}{N}}$. Then, $\sum_{m=0}^{n} \alpha_m = D_N(\widetilde{h})^2\Delta t(T + \| \frac{du}{dt} \|^2_{L^2(L^2(\Omega)^2)})$.

Generally, we have

$$
d(\frac{\sigma^m}{\Delta t}, \eta^{m+1}) = -\frac{1}{\Delta t}(\sigma^m, \eta^{m+1}) \geq -C(\frac{\widetilde{h}^2 \| \nabla\eta^{m+1} \|_0^2}{\Delta t} + \frac{\Delta t}{\widetilde{h}^2} \| \frac{\sigma^m}{\Delta t} \|_0^2).
$$

From [18–20], the term $\frac{1}{\Delta t}G(\sigma^{m+1}, \sigma^{m+1})$ can be treated as below:

$$
C\frac{\widetilde{h}^2 \| \nabla\sigma^{m+1} \|_0^2}{\Delta t} \leq \frac{1}{\Delta t} \| (I - IH_{\widetilde{h}})\nabla\sigma^{m+1} \|_0^2 .
$$

For $2C < \frac{\widetilde{h}^2}{\Delta t} < 1$, choosing $C_{\min} = \{1 - \frac{\widetilde{h}^2}{\Delta t}, 1 - \frac{\Delta t}{\widetilde{h}^2}\}$. and simplying (3.6) yields

$$
\begin{aligned}
&(\frac{\nu}{2\Delta t} + \frac{1}{2\Delta t})(\| \nabla\sigma^{m+1} \|_0^2 - \| \nabla\sigma^m \|_0^2) + C_{\min} \| \frac{\sigma^{m+1}}{\Delta t} \|_0^2 + C_{\min} \| \frac{\sigma^m}{\Delta t} \|_0^2 + \frac{\nu}{2} \mid \frac{\sigma^{m+1}-\sigma^m}{(\Delta t)^{\frac{1}{2}}} \mid_1^2 \\
&\leq \varepsilon_3 \| \frac{\sigma^{m+1}-\sigma^m}{\Delta t} \|_0^2 + C\Delta t(\| D_t^2 u \|^2_{L^2(t_m,t_{m+1};L^2(\Omega)^2)} + \| \frac{du}{dt} \|^2_{L^2(t_m,t_{m+1};L^2(\Omega)^2)}) \\
&+\varepsilon_4 \mid \frac{\sigma^{m+1}-\sigma^m}{(\Delta t)^{\frac{1}{2}}} \mid_1^2 + C(1+\frac{\alpha_m}{\Delta t}) \| \delta \|^2_{L^\infty(\widetilde{h}^1(\Omega)^2)} + C \| \nabla\sigma \|_0^2 \\
&+C(1+\frac{\alpha_m}{\Delta t}) \| \nabla\sigma^m \|_0^2 . \qquad (3.7)
\end{aligned}
$$

We begin by multiplying Eq (3.7) by $2\Delta t$, followed by summing the result over index m from 0 to n. With the parameter choices $\varepsilon_1 = \frac{1}{4T}$ and $\varepsilon_2 = \frac{\nu}{2}$, the recurrence relation is obtained. With $\varepsilon_3 = \frac{1}{2}C_{\min}, \varepsilon_4 = \frac{\nu}{4}$, we obtain

$$
\begin{aligned}
&\| \nabla\sigma^{n+1} \|_0^2 + C_{\min}\Delta t \sum_{m=0}^{n} \| \tfrac{\sigma^{m+1}}{\Delta t} \|_0^2 + C_{\min}\Delta t \sum_{m=0}^{n} \| \tfrac{\sigma^{m}}{\Delta t} \|_0^2 + \Delta t \sum_{m=0}^{n} | \tfrac{\sigma^{m+1}-\sigma^{m}}{(\Delta t)^{\frac{1}{2}}} |_1^2 \\
&\le C\Delta t^2(\| D_t^2 u \|^2_{L^2(L^2(\Omega)^2)} + \| \tfrac{du}{dt} \|^2_{L^2(L^2(\Omega)^2)}) \\
&+C(1 + \sum_{m=0}^{n} \alpha_m) \| \delta \|^2_{L^\infty(H^1(\Omega)^2)} + C \| \tfrac{d\delta}{dt} \|^2_{L^2(L^2(\Omega)^2)}) + C\Delta t \sum_{m=0}^{n} \| e^m \|_0^2 \\
&+C \sum_{m=0}^{n} (\Delta t + \alpha_m) \| \nabla\sigma^m \|_0^2;
\end{aligned}
$$

together with the discrete Grönwall's lemma and Lemma 4.1,

$$
\begin{aligned}
&\| \nabla e^{n+1} \|_0^2 \le 2 \| \nabla\delta^{n+1} \|_0^2 + 2 \| \nabla\sigma^{n+1} \|_0^2 \\
&\le C\Delta t^2(\| D_t^2 u \|^2_{L^2(L^2(\Omega)^2)} + \| \tfrac{du}{dt} \|^2_{L^2(L^2(\Omega)^2)}) \\
&+Ch^2(\| u \|^2_{L^\infty(\widetilde{h}^2(\Omega)^2)} + \| \tfrac{du}{dt} \|^2_{L^2(\widetilde{h}^2(\Omega)^2)} + \| p \|^2_{L^\infty(\widetilde{h}^1(\Omega))} \\
&+ \| \tfrac{dp}{dt} \|^2_{L^2(\widetilde{h}^1(\Omega))}) + C\Delta t \sum_{m=0}^{n} \| e^m \|_0^2 .
\end{aligned}
$$

By the Poincaré–Friedrichs inequality, $\| e^n \|_0 \le C \| \nabla e^n \|_0$, and the discrete Grönwall's lemma, we complete the proof of Theorem 4.2.

Theorem 4.3 Under regularity hypotheses, we have

$$\| p - p_{\widetilde{h}} \|_{L^2(0,T,L^2(\Omega))} \le C(\Delta t + \widetilde{h}).$$

Proof. From the definition B_1 and (3.1), we have

$$
\begin{aligned}
&B_1(\sigma^{m+1}, \eta^{m+1}; (v_{\widetilde{h}}, q_{\widetilde{h}})) = (D_t u(\cdot, t_{m+1}), v_{\widetilde{h}}) - (d_t u(\cdot, t_{m+1}), v_{\widetilde{h}}) \\
&+(d_t\delta^{m+1}, v_{\widetilde{h}}) - (d_t\sigma^{m+1}, v_{\widetilde{h}}).
\end{aligned} \tag{3.8}
$$

From the Theorem 3.1, we get

$$
\begin{aligned}
&\beta(\| \sigma^{m+1} \|_1 + \| \eta^{m+1} \|_0) \le \sup_{(v_{\widetilde{h}}, q_{\widetilde{h}}) \in (X_{\widetilde{h}}, M_{\widetilde{h}})} \frac{B((\sigma^{m+1}, \eta^{m+1}); (v_{\widetilde{h}}, q_{\widetilde{h}}))}{\| v_{\widetilde{h}} \|_1 + \| q_{\widetilde{h}} \|_0} \\
&\le \sup_{(v_{\widetilde{h}}, q_{\widetilde{h}}) \in (X_{\widetilde{h}}, M_{\widetilde{h}})} \frac{(D_t u(\cdot, t_{m+1}) - d_t u(\cdot, t_{m+1}), v_{\widetilde{h}}) + (d_t\delta^{m+1}, v_{\widetilde{h}}) - (d_t\sigma^{m+1}, v_{\widetilde{h}})}{\| v_{\widetilde{h}} \|_1 + \| q_{\widetilde{h}} \|_0}.
\end{aligned} \tag{3.9}
$$

Furthermore, we have

$$
\begin{aligned}
&\| \eta^{m+1} \|_0 + \| (I - II_{\widetilde{h}})\nabla\sigma^{m+1} \|_0^2 \le \| D_t u(\cdot, t_{m+1}) - \frac{u(\cdot, t_{m+1}) - u(X(\cdot, t_{m+1}; t_m), t_m)}{\Delta t} \|_0 \\
&+ \| \frac{u(X(\cdot, t_{m+1}; t_m), t_m) - u(X_h^m(\cdot, t_{m+1}; t_m), t_m)}{\Delta t} \|_0 \\
&+ \| \frac{\delta(\cdot, t_{m+1}) - \delta(\cdot, t_m)}{\Delta t} \|_0 + \| \frac{\delta(\cdot, t_m) - \delta(X(\cdot, t_{m+1}; t_m), t_m)}{\Delta t} \|_{-1} \\
&+C \| \frac{\delta(X(\cdot, t_{m+1}; t_m), t_m) - \delta(X_{\widetilde{h}}^m(\cdot, t_{m+1}; t_m), t_m)}{\Delta t} \|_{0,1} + \| \frac{\sigma^m(\cdot) - \sigma^m(X(\cdot, t_{m+1}; t_m))}{\Delta t} \|_{-1} \\
&+C \| \frac{\sigma^m(X(\cdot, t_{m+1}; t_m)) - \sigma^m(X_{\widetilde{h}}^m(\cdot, t_{m+1}; t_m))}{\Delta t} \|_{0,1} + \| \frac{\sigma^{m+1}}{\Delta t} \|_0 + \| \frac{\sigma^m}{\Delta t} \|_0 .
\end{aligned} \tag{3.10}
$$

By a similar argument with the proof of Theorems 4.1 and 4.2 together with Theorem 3.1, we obtain Theorem 4.3.

4. Some classical finite element algorithms and numerical experiments

Algorithm 2. Simple two-level stabilized finite element approximation [21].

Step I: Solve the fully nonlinear equations on a coarse grid.

Solve the stabilized Navier–Stokes problem on a coarse mesh, and find $(u_H, p_H) \in (X_H, M_H)$ such that for all $(v_H, q_H) \in (X_H, M_H)$,

$$B_0((u_H, p_H); (v_H, q_H)) + b(u_H, u_H, v_H) = (f, v_H).$$

Step II: Linearize the problem on a fine grid by inserting the value computed at Step *I* into the nonlinear term

$$S_{\widetilde{h}} = I - \Pi, \quad G_2(p, q) = (S_{\widetilde{h}} p, S_{\widetilde{h}} q),$$

with I as the identity operator and the local pressure projection $\Pi : L^2(\Omega) \to R_0$. Note that R_0 is a piecewise constant on set K.

Solve the stabilized Stokes problem on a fine mesh and find $(u_h, p_h) \in (X_h, M_h)$ such that for all $(v_h, q_h) \in (X_h, M_h)$,

$$B_2((u^h, p^h); (v_h, q_h)) + b(u_H, u_H, v_h) = (f, v_h).$$

$$B_2((u_{\widetilde{h}}, p_{\widetilde{h}}); (v_{\widetilde{h}}, q_{\widetilde{h}})) = B_0((u_{\widetilde{h}}, p_{\widetilde{h}}); (v_{\widetilde{h}}, q_{\widetilde{h}})) + G_2(p_{\widetilde{h}}, q_{\widetilde{h}}).$$

where the bilinear form $G_1(\cdot, \cdot)$ can be defined by the local Gauss integral technique (see [22]) by the bounded operator $S_{\widetilde{h}} : L^2(\Omega) \to L^2(\Omega)$.

Algorithm 3. Common variational multiscale (VMS) method [23].

$$\begin{gathered}(\tfrac{\partial u_{\widetilde{h}}}{\partial t}, v_{\widetilde{h}}) + B_3((u_{\widetilde{h}}^{m+1}, p_{\widetilde{h}}^{m+1}) - \alpha(g_{\widetilde{h}}, \nabla v_{\widetilde{h}}) + b(u_{\widetilde{h}}, u_{\widetilde{h}}, v_{\widetilde{h}}) = (f, v_{\widetilde{h}}) \quad \forall v_{\widetilde{h}} \in X_{\widetilde{h}}, \\ d(q_{\widetilde{h}}, u_{\widetilde{h}}) = 0 \quad \forall q_{\widetilde{h}} \in Q_{\widetilde{h}}, \\ (g_{\widetilde{h}} - \nabla u_{\widetilde{h}}, l_{\widetilde{h}}) = 0 \quad \forall l_{\widetilde{h}} \in L_{\widetilde{h}}. \end{gathered} \tag{4.1}$$

Here,

$$B_3((u_{\widetilde{h}}^{m+1}, p_{\widetilde{h}}^{m+1}) = B_0((u_{\widetilde{h}}^{m+1}, p_{\widetilde{h}}^{m+1}) + \alpha a(u_{\widetilde{h}}, v_{\widetilde{h}}).$$

This system is determined by the choices of $L_{\widetilde{h}}$ and α. The stabilization parameter α in this scheme acts only on the small scales.

The corresponding solution (u,p) of problem (1.1) will be assumed to satisfy the following regularity hypotheses.

Table 1. Algorithm 1. CFEM based on two Gauss integrations for Re=1,000,000.

$\frac{1}{h}$	$\frac{\|u-u_h\|_0}{\|u\|_0}$	order	$\frac{\|u-u_h\|_1}{\|u\|_1}$	order	$\frac{\|p-p_h\|_0}{\|p\|_0}$	order	CPU(s)
15	0.0348973	/	0.234885	/	0.0221604	/	1.096
30	0.00823913	4.1651	0.113878	2.0889	0.00864719	2.7154	23.683
60	0.00201651	4.0613	0.0564433	2.0252	0.00372448	2.4304	462.306
120	0.000498967	4.0297	0.0281015	2.0123	0.00171521	2.2373	13398.1

Table 2. Algorithm 2. Simple two-level stabilized finite element approximation for Re=1,000,000.

$\frac{1}{h}$	$\frac{1}{H}$	$\frac{\|u-u_h\|_0}{\|u\|_0}$	order	$\frac{\|u-u_h\|_1}{\|u\|_1}$	order	$\frac{\|p-p_h\|_0}{\|p\|_0}$	order	CPU(s)
15	10	0.034991	/	0.234988	/	0.152727	/	1.117
30	20	0.0087213	4.0087	0.114269	2.0803	0.0790345	1.9008	20.386
60	40	0.0035672	2.5795	0.0577235	1.9704	0.0401588	1.9535	558.178
120	80	0.0030149	0.4854	0.0322965	1.6756	0.0202463	1.9761	21833

Table 3. Algorithm 3. Common variational multiscale (VMS) method for Re=1,000,000.

$\frac{1}{h}$	$\frac{\|u-u_h\|_0}{\|u\|_0}$	order	$\frac{\|u-u_h\|_1}{\|u\|_1}$	order	$\frac{\|p-p_h\|_0}{\|p\|_0}$	order	CPU(s)
15	0.0348975	/	0.234885	/	0.0221614	/	1.829
30	0.00823943	4.1651	0.113878	2.0889	0.00864759	2.7154	39.2
60	0.00201951	4.0613	0.0564433	2.0252	0.00372448	2.4304	779.743
120	0.000498967	4.0297	0.0281015	2.0123	0.00171521	2.2373	22512.3

Table 4. CPU for Algorithm 1; VMS vs Algorithm 3; CFEM based on two Gauss integrations.

$1/h$	$t_{Algorithm3}$	$t_{Algorithm4}$	$save_{times}$
15	1.829	1.096	40.0765446 %
30	39.2	23.683	39.5841837 %
60	779.743	462.306	40.7104649 %
120	22512.3	13398.1	40.4854235 %

As can be seen from Tables 1, 3 and 4, the time discretization of Algorithm 3 includes an unsteady term $\frac{\partial \boldsymbol{u}_{\bar{h}}}{\partial t}$ and a nonlinear convective term $b(\boldsymbol{u}_{\bar{h}}, \boldsymbol{u}_{\bar{h}}, \boldsymbol{v}_{\bar{h}})$, adopting an implicit scheme (evident from $\boldsymbol{u}_{\bar{h}}^{m+1}$): The implicit scheme requires iterative linearization of the nonlinear term (e.g., the Newton–Raphson method), with the coupled system (velocity + pressure + small-scale variables) reassembled in each iteration.

In contrast, the conventional method of characteristics has no additional stabilization terms: Its stability comes from the accurate discretization of the convective term via characteristic line tracing (essentially an "upwind-type discretization"). No artificial stabilization terms or tensor projections

are needed, only basic interpolation operations (for node value interpolation during trajectory tracing), resulting in much lower computational overhead.

The time discretization of the conventional method of characteristics is usually explicit or semiexplicit: The convective term is discretized explicitly via characteristic line tracing (directly using the velocity field from the previous time step to compute particle trajectories), requiring no iteration, and the diffusion term can be explicit or implicit, but the system scale is still much smaller than VMS without additional unknowns, making iterative overhead negligible.

As can be seen from Table 2, the high Reynolds number amplifies nonlinear errors; with $Re = 10^6$, the flow is characterized by a high Reynolds number where the convective term dominates as inertial forces are much larger than viscous forces, leading to extremely strong nonlinear effects. At this point, using the coarse-grid solution u_H to approximate the fine-grid solution u_h results in a sharp amplification of the linearization error of the convective term. Moreover, as h is refined (the fine grid is more capable of capturing local structures such as strong shear and vortices), the "approximation accuracy" of u_H fails to keep pace with the "discretization accuracy" of the fine grid, leading to a continuous decline in the convergence order.

As can be seen from Table 3, the core idea of VMS is to separate large-scale and small-scale effects of the flow. It introduces an *additional small-scale unknown* $g_{\widetilde{h}} \in L_{\widetilde{h}}$ related to the velocity deformation tensor to stabilize high-Reynolds number flows, leading to a drastic increase in the number of degrees of freedom (DOFs) of the solved system. Basic unknowns include the velocity $\boldsymbol{u}_{\widetilde{h}} \in X_{\widetilde{h}}$ (d-dimensional vector, $d = 2$), and pressure, $p_{\widetilde{h}} \in Q_{\widetilde{h}}$ (scalar). An additional unknown is small-scale deformation tensor-related variable $g_{\widetilde{h}} \in L_{\widetilde{h}}$ ($d \times d$ tensor space, e.g., 3 independent components per grid node in 2D).

The final solved system is a coupled equation set of number of velocity components plus pressure plus a number of small-scale tensor components, with a scale of

$$\text{System Size} = O\left(N \cdot (d + 1 + d^2)\right)'$$

where N is the number of velocity grid nodes.

The stabilization term B_3 in Algorithm 3 consists of the basic bilinear form B_0 (viscous + pressure terms) and an additional stabilization term $\alpha a(\boldsymbol{u}_{\widetilde{h}}, \boldsymbol{v}_{\widetilde{h}})$. The constraint equation for the small-scale variable $g_{\widetilde{h}}$,

$$(g_{\widetilde{h}} - \nabla \boldsymbol{u}_{\widetilde{h}}, l_{\widetilde{h}}) = 0 \quad \forall l_{\widetilde{h}} \in L_{\widetilde{h}}$$

is essentially an orthogonal projection of the difference between the small-scale deformation tensor and velocity gradient onto $L_{\widetilde{h}}$. It requires per element ($\Omega_e \in \tau_{\widetilde{h}}$) computations as follows:

(i) Calculation of the velocity gradient $\nabla \boldsymbol{u}_{\widetilde{h}}$ (tensor operation with multiple components per element in 2D);

(ii) Projection matrix computation via Gauss quadrature (high-order quadrature is often required for accuracy, similar to the dual-integration logic in Algorithm 2);

(iii) Assembly of local integration results into the global system.

Consider Eq (1.1) in the domain $\Omega = [0, 1] \times [0, 1]$ with the following exact solutions:

$$u(x, y) = (u_1(x, y), u_2(x, y)), \quad p(x, y) = 10(2x - 1)(2y - 1)\cos(t),$$

$$u_1(x, y) = 10x^2y(x - 1)^2(y - 1)(2y - 1)\cos(t), \quad u_2(x, y) = -10xy^2(2x - 1)(y - 1)\cos(t).$$

For numerical verification, a time step size of $\Delta t = 0.8h^2$ is adopted. Relative errors, convergence rates, and computational costs of the characteristic finite element method with two local Gaussian integrations are summarized in Table 1, and Tables 2 and 3 provide reference results from several classical finite element schemes. Comparative analysis confirms the superior accuracy and efficiency of the proposed characteristic method with two local Gaussian integrations.

As evidenced in Tables 3 and 4, the stabilization terms constructed via two local Gaussian integrations induce superconvergence phenomena in both the variational multiscale and characteristic finite element frameworks, significantly enhancing numerical accuracy. Figure 1 further illustrates the stabilized convergence behavior of the proposed method, which maintains a consistent error reduction rate under mesh refinement, unlike the standard characteristic method, whose convergence deteriorates progressively.

The lid-driven cavity flow is additionally simulated following the benchmark configuration in [24]. Our results in Figures 2–11 align closely with the classical data reported by Ghia et al. [24]. Streamline patterns in Figures 7–11 reveal that elevated Reynolds numbers lead to increased vortex generation, indicating that strong inertial effects amplify small perturbations and trigger flow instability. This mechanism fosters multiscale vortex formation and evolution, ultimately culminating in turbulent flow regimes.

Figures 12–15 present a classic numerical simulation of flow around a cylinder for which the Reynolds number is set to $Re = 600$. At 25 minutes, both the velocity and pressure fields exhibit a stable pattern, with a pair of symmetric vortices appearing behind the cylinder. By 50 minutes, slight fluctuations begin to emerge in the otherwise stable flow. When the time reaches 75 minutes, the flow becomes unstable, leading to large-scale oscillations. At 100 minutes, vortex shedding occurs in the system, forming the well-known **Kármán** vortex street [25, 26].

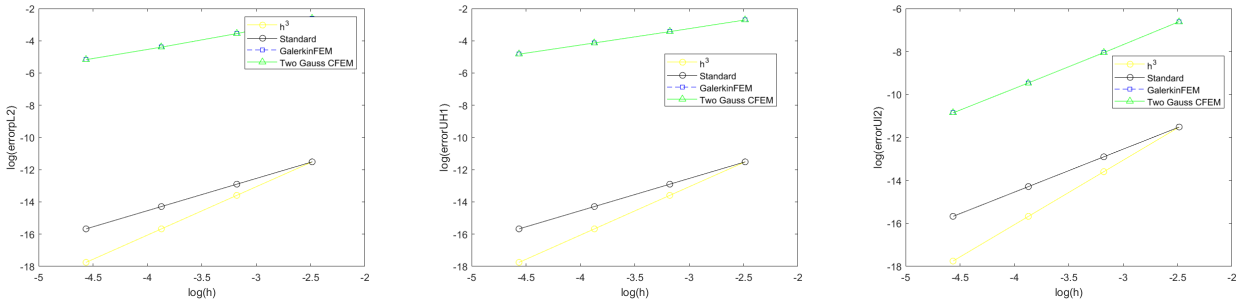

Figure 1. Convergence analysis for the velocity and pressure using different methods. Left: L2 error for the velocity; middle: H1 error for the velocity; right: L2 error for the pressure.

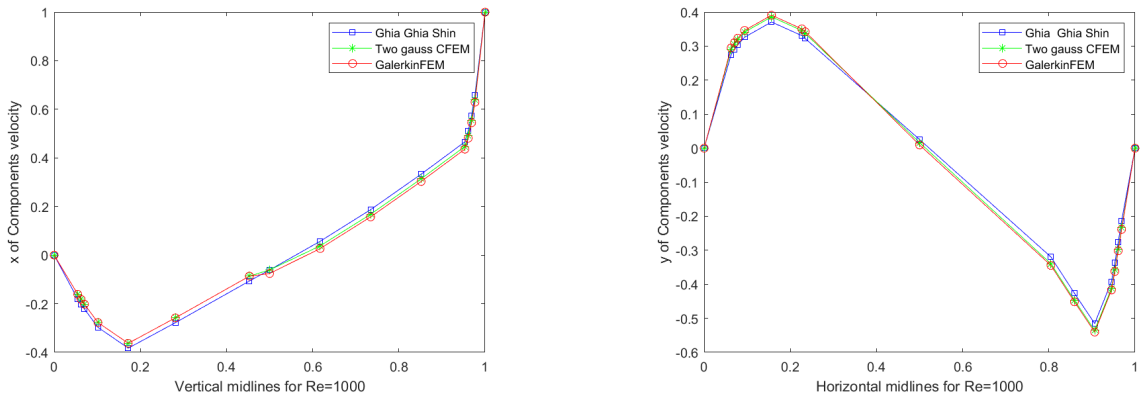

Figure 2. At RE = 1000, the left and right figures show vertical midlines and horizontal midlines, respectively.

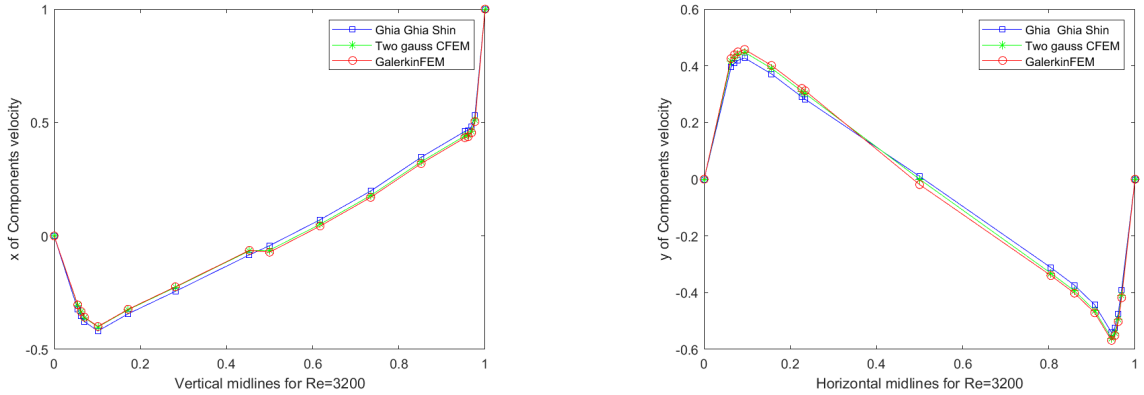

Figure 3. At RE = 3200, the left and right figures show vertical midlines and horizontal midlines, respectively.

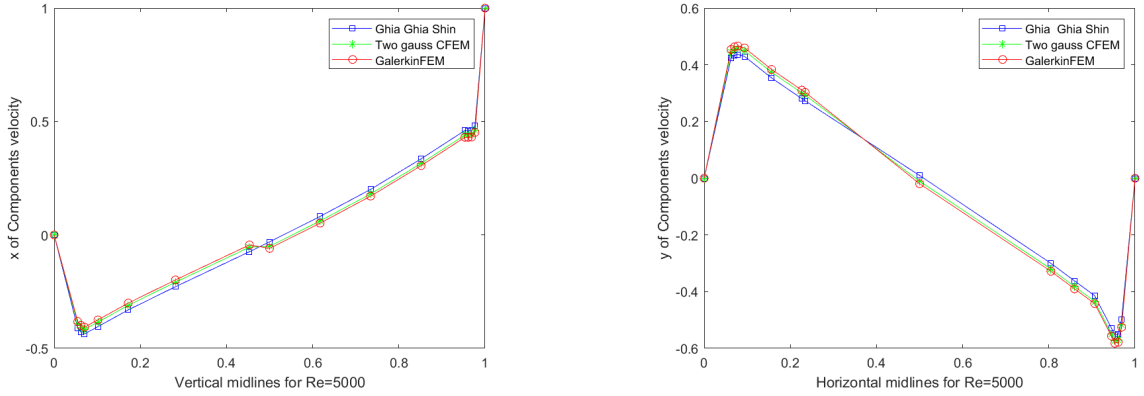

Figure 4. At RE = 5000, the left and right figures show vertical midlines and horizontal midlines, respectively.

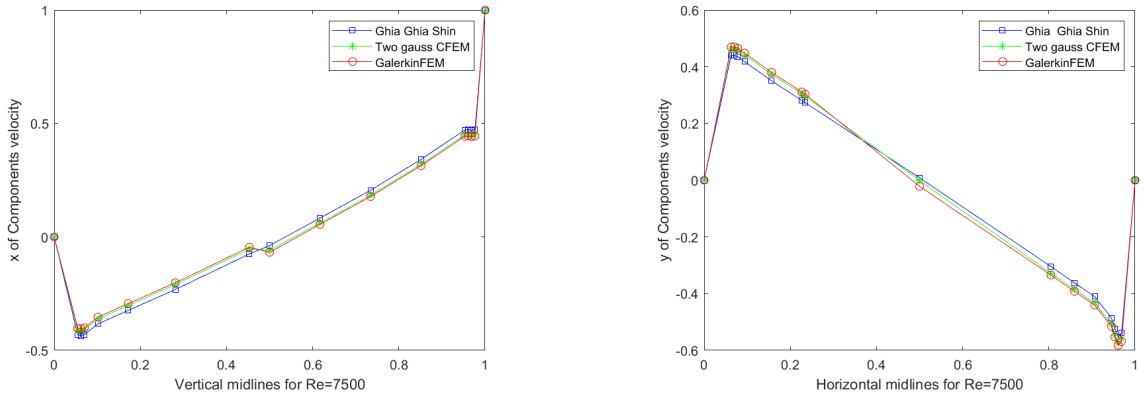

Figure 5. At RE = 7500, the left and right figures show vertical midlines and horizontal midlines, respectively.

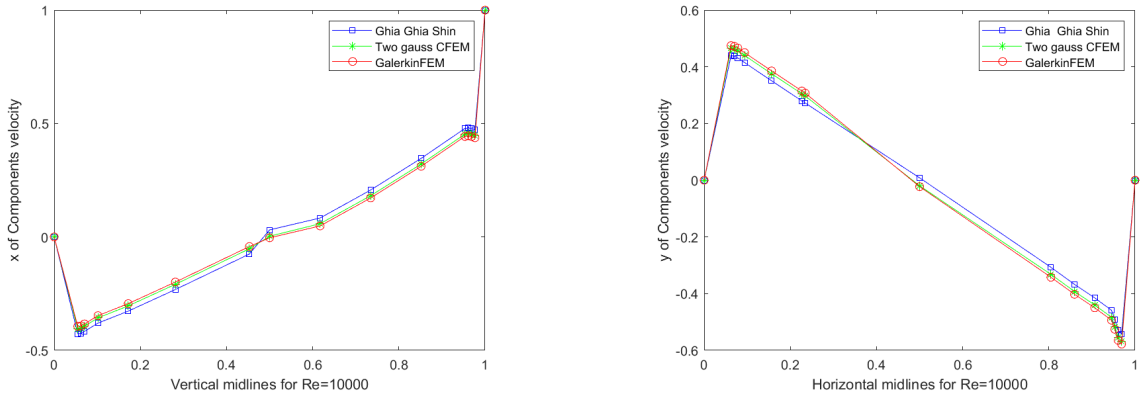

Figure 6. At RE = 10 000, the left and right figures show vertical midlines and horizontal midlines, respectively.

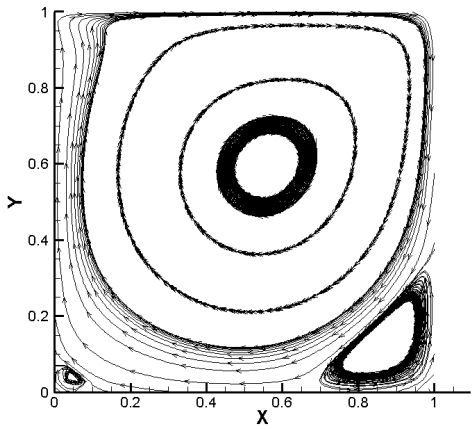

Figure 7. At RE = 1000, the figure shows velocity streamlines.

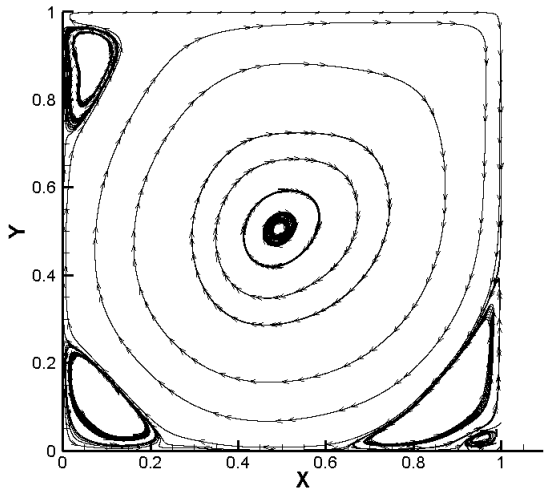

Figure 8. At RE = 3200, the figure shows velocity streamlines.

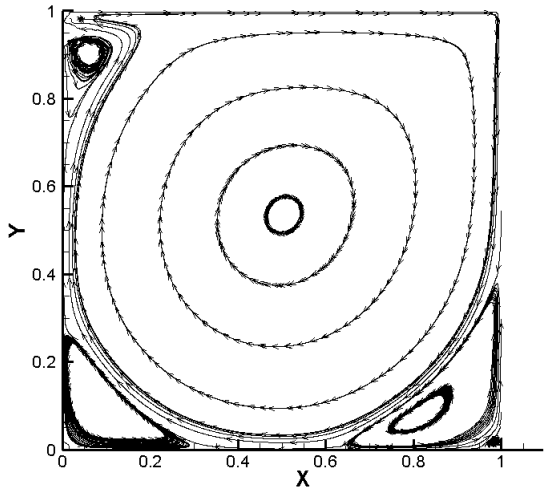

Figure 9. At RE = 5000, the figure shows velocity streamlines.

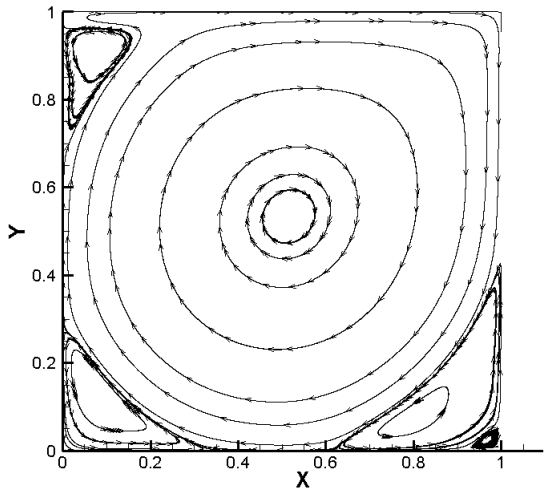

Figure 10. At RE = 7500, the figure shows velocity streamlines.

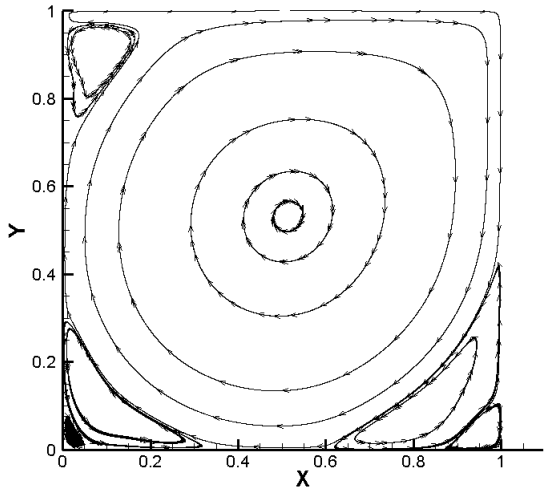

Figure 11. At RE = 10 000, the figure shows velocity streamlines.

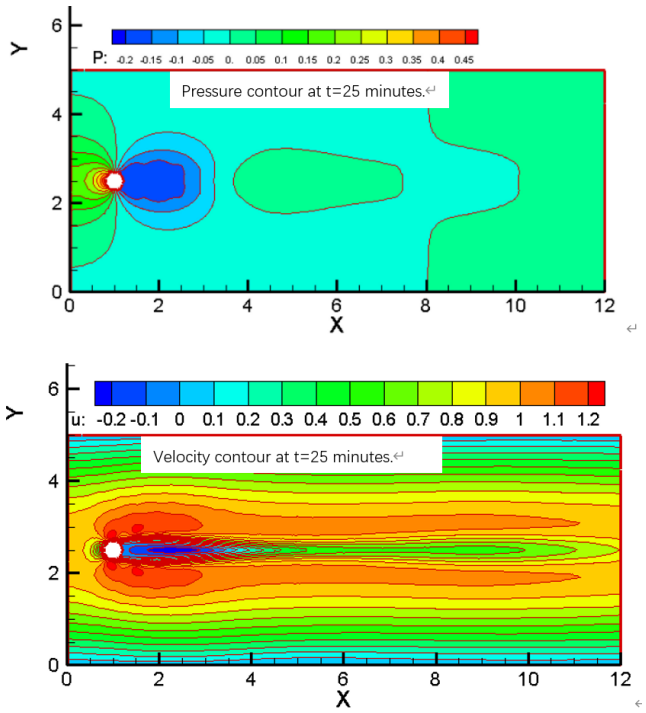

Figure 12. At RE = 600 and t=25 minutes, the top figure shows the pressure contour plot, and the bottom figure shows the velocity contour plot.

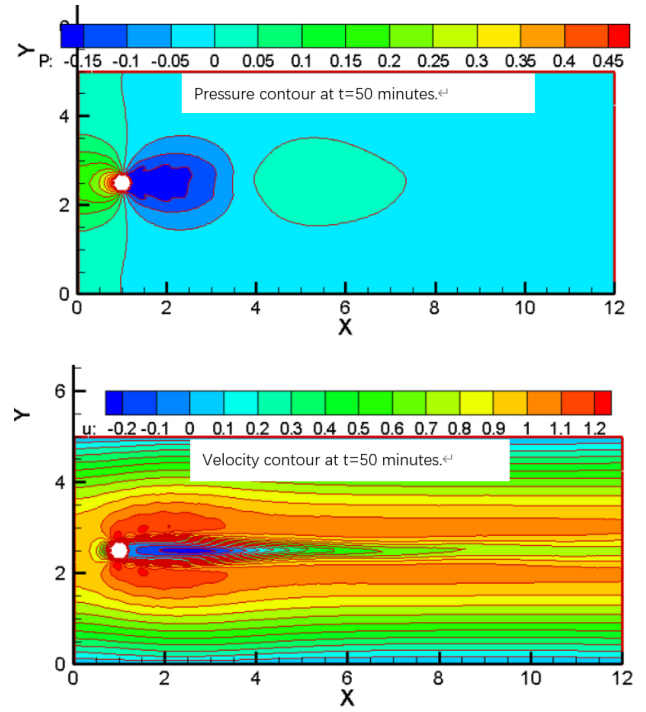

Figure 13. At RE = 600 and t = 50 minutes, the top figure shows the pressure contour plot, and the bottom figure shows the velocity contour plot.

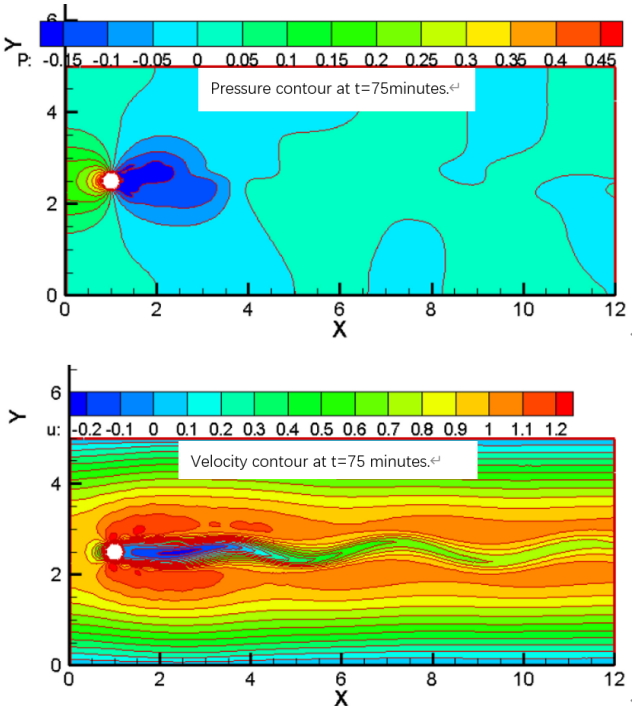

Figure 14. At RE = 600 and t = 75 minutes, the top figure shows the pressure contour plot, and the bottom figure shows the velocity contour plot.

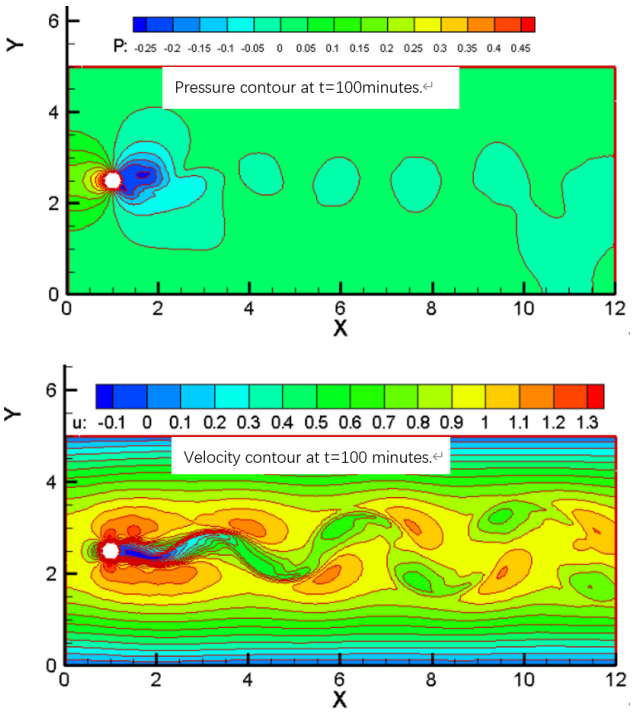

Figure 15. At RE = 600 and t = 100 minutes, the top figure shows the pressure contour plot, and the bottom figure shows the velocity contour plot.

5. Conclusions

Our proposed characteristics finite element method is based on two local Gauss integrations. It not only retains the speed advantage of the traditional CFEM but also solves the problems of instability and low convergence order of the CFEM under high Reynolds numbers through localized stabilization terms, ultimately achieving a triple balance of accuracy, stability, and efficiency.

The improved algorithm does not change the core design logic of decoupling convection and diffusion effects via characteristic line tracing, which is the fundamental reason for its low computational cost: The improved algorithm only adds local stabilization terms based on two Gaussian integrations but does not introduce new global unknowns. The solved system still consists of only two core unknowns: velocity $\boldsymbol{u}$ and pressure p, with a degree of freedom (CFEM) scale of $O(N \cdot (d + 1))$, where $d = 2$ corresponds to 2D flows.

Compared with the VMS method, with a DOF scale of $O(N \cdot (d + 1 + d^2))$ that requires additional solution of small-scale tensor variables, the system scale of the improved algorithm is reduced by an order of magnitude, directly bringing two key advantages:

i. Faster matrix assembly: The stiffness matrix is a sparse matrix with a low proportion of nonzero elements (small fill rate).
ii. Efficient linear solution: When solving the diffusion term and pressure Poisson equation, the number of iterations is small, and the cost of matrix–vector multiplication per iteration is low (e.g., iterative methods such as CG and GMRES achieve extremely high efficiency).

Use of AI tools declaration

The authors declare they have not used Artificial Intelligence (AI) tools in the creation of this article.

Conflict of interest

The authors declare there are no conflicts of interest.

References

1. L. Zuo, G. Du, Two stabilized finite element methods based on local polynomial pressure projection for the steady-state Navier-Stokes-Darcy problem, *Finite Elem. Anal. Des.*, **251** (2025), 104420. https://doi.org/10.1016/j.finel.2025.104420
2. H. Xu, Y. He, Some iterative finite element methods for steady Navier-Stokes equations with different viscosities, *J. Comput. Phys.*, **232** (2013), 136–152. https://doi.org/10.1016/j.jcp.2012.07.020
3. T. Frachon, S. Zahedi, A cut finite element method for incompressible two-phase Navier-Stokes flows, *J. Comput. Phys.*, **384** (2019), 77–98. https://doi.org/10.1016/j.jcp.2019.01.028
4. L. Li, A split-step finite-element method for incompressible Navier-Stokes equations with high-order accuracy up to the boundary, *J. Comput. Phys.*, **408** (2020), 109274. https://doi.org/10.1016/j.jcp.2020.109274

5. B. Duan, B. Li, Z. Yang, An energy diminishing arbitrary Lagrangian-Eulerian finite element method for two-phase Navier-Stokes flow, *J. Comput. Phys.*, **461** (2022), 111215. https://doi.org/10.1016/j.jcp.2022.111215
6. S. Yang, H. Tian, A posteriori error estimates and time adaptivity for fully discrete finite element method for the incompressible Navier-Stokes equations, *Appl. Numer. Math.*, **216** (2025), 17–38. https://doi.org/10.1016/j.apnum.2025.05.001
7. N. Zhu, H. Rui, A Petrov-Galerkin immersed finite element method for steady Navier-Stokes interface problem with non-homogeneous jump conditions, *J. Comput. Appl. Math.*, **445** (2024), 115815. https://doi.org/10.1016/j.cam.2024.115815
8. Y. Jiang, L. Mei, H. Wei, A finite element variational multiscale method for incompressible flow, *Appl. Math. Comput.*, **266** (2015), 374–384. https://doi.org/10.1016/j.amc.2015.05.055
9. V. John, S. Kaya, A finite element variational multiscale method for the Navier-Stokes equations, *SIAM J. Sci. Comput.*, **26** (2005), 1485–1503. https://doi.org/10.1137/030601533
10. V. A. B. Narayanan, N. Zabaras, Variational multiscale stabilized FEM formulations for transport equations: stochastic advection-diffusion and incompressible stochastic Navier-Stokes equations, *J. Comput. Phys.*, **202** (2005), 94–133. https://doi.org/10.1016/j.jcp.2004.06.019
11. X. H. Zhang, H. Xiang, Variational multiscale element free Galerkin method for convection-diffusion-reaction equation with small diffusion, *Eng. Anal. Boundary Elem.*, **46** (2014), 85–92. https://doi.org/10.1016/j.enganabound.2014.05.010
12. C. E. Wasberg, T. Gjesdal, B. A. P. Reif, Ø. Andreassen, Variational multiscale turbulence modelling in a high order spectral element method, *J. Comput. Phys.*, **228** (2009), 7333–7356. https://doi.org/10.1016/j.jcp.2009.06.029
13. V. John, S. Kaya, A. Kindl, Finite element error analysis for a projection-based variational multiscale method with nonlinear eddy viscosity, *J. Math. Anal. Appl.*, **344** (2008), 627–641. https://doi.org/10.1016/j.jmaa.2008.03.015
14. Z. H. Ge, J. J. Yan, Analysis of multiscale finite element method for the stationary Navier-Stokes equations, *Nonlinear Anal. Real World Appl.*, **13** (2012), 385–394. https://doi.org/10.1016/j.nonrwa.2011.07.050
15. P. B. Bochev, C. R. Dohrmann, M. D. Gunzburger, Stabilized of low-order mixed finite element for the stokes equations,*SIAM J. Numer. Anal.*, **44** (2006), 82–101. https://doi.org/10.1137/S0036142905444482
16. H. B. De Oliveira, N. D. Lopes, Continuous/Discontinuous finite element approximation of a 2d Navier-Stokes problem arising in fluid confinement, *Int. J. Numer. Anal. Model.*, **21** (2024), 315–352. https://doi.org/10.4208/ijnam2024-1013
17. J. M. Connors, M. Gaiewski, An H1-conforming solenoidal basis for velocity computation on Powell-Sabin splits for the Stokes problem, *Int. J. Numer. Anal. Model.*, **21** (2024), 181–200. https://doi.org/10.4208/ijnam2024-1007
18. W. Layton, A connection between subgrid scale eddy viscosity and mixed methods, *Appl. Math. Comput.*, **133** (2002), 147–157. https://doi.org/10.1016/S0096-3003(01)00228-4

19. M. Gunzburger, *Finite Element Methods for Viscous Incompressible Flows: A Guide to Theory, Practice, and Algorithms*, Academic Press, Boston, 1989.

20. H. E. Jia, K. T. Li, S. H. Liu, Characteristic stabilized finite element method for the transient Navier-Stokes equations, *Comput. Methods Appl. Mech. Eng.*, **199** (2010), 2996–3004. https://doi.org/10.1016/j.cma.2010.06.010

21. J. Li, Investigations on two kinds of two-level stabilized finite element methods for the stationary Navier–Stokes equations, *Appl. Math. Comput.*, **182** (2006), 1470–1481. https://doi.org/10.1016/j.amc.2006.05.034

22. J. Li, Y. He, A stabilized finite element method based on two local Gauss integrations for the Stokes equations, *J. Comput. Appl. Math.*, **214** (2008), 58–65. https://doi.org/10.1016/j.cam.2007.02.015

23. V. John, S. Kaya, A finite element variational multiscale method for the Navier–Stokes equations, SIAM J. Sci. Comput. 26 (2005) 1485–1503.

24. U. Ghia, K. N. Ghia, C. T. Shin, High-Re solutions for incompressible flow using the Navier-Stokes equations and a multigrid method, *J. Comput. Phys.*, **48** (1982), 387–411. https://doi.org/10.1016/0021-9991(82)90058-4

25. A. Scala, G. Paolillo, C. S. Greco, T. Astarita, G. Cardone, Genetically-based active flow control of a circular cylinder wake via synthetic jets, *Exp. Therm Fluid Sci.*, **162** (2025), 111362. https://doi.org/10.1016/j.expthermflusci.2024.111362

26. S. Muddada, K. Hariharan, V. S. Sanapala, B. S. V. Patnaik, Circular cylinder wakes and their control under the influence of oscillatory flows: A numerical study, *J. Ocean. Eng. Sci.*, **6** (2021), 389–399. https://doi.org/10.1016/j.joes.2021.04.002

AIMS Press